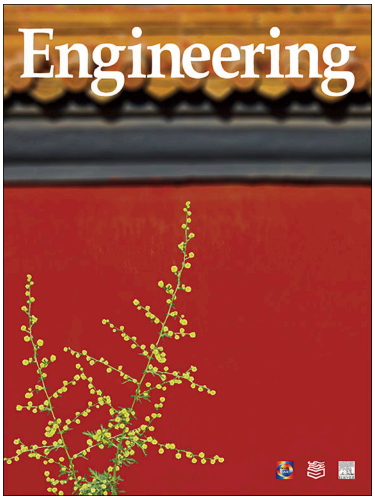

Article

Continuous Joule Heating for Scalable and General Fusion Ternary Metal Oxides with Triple-Active Fenton-Like Activity

Xiangdong Zhu, Beibei Xiao, Fengbo Yu, Chao Jia, Liming Sun, Shicheng Zhang, Lianli Wang, Peixin Cui, Liang Wang, Xiaoguang Duan, Shaobin Wang, Yujun Wang

PII: S2095-8099(25)00298-X
DOI: https://doi.org/10.1016/j.eng.2025.06.004
Reference: ENG 1921

To appear in: *Engineering*

Received Date: 12 September 2024
Revised Date: 4 May 2025
Accepted Date: 5 June 2025

Please cite this article as: X. Zhu, B. Xiao, F. Yu, C. Jia, L. Sun, S. Zhang, L. Wang, P. Cui, L. Wang, X. Duan, S. Wang, Y. Wang, Continuous Joule Heating for Scalable and General Fusion Ternary Metal Oxides with Triple-Active Fenton-Like Activity, *Engineering* (2025), doi: https://doi.org/10.1016/j.eng.2025.06.004

Research

Environmental Engineering—Article

Continuous Joule Heating for Scalable and General Fusion Ternary Metal Oxides with Triple-Active Fenton-Like Activity

Xiangdong Zhu [a,b,c], Beibei Xiao [d], Fengbo Yu [a,b,*], Chao Jia [a,b], Liming Sun [a,b], Shicheng Zhang [b], Lianli Wang [e], Peixin Cui [a,c], Liang Wang [d], Xiaoguang Duan [f], Shaobin Wang [f], Yujun Wang [a,c,*]

[a] *State Key Laboratory of Soil and Sustainable Agriculture, Institute of Soil Science, Chinese Academy of Sciences, Nanjing 210018, China.*

[b] *Department of Environmental Science and Engineering, Fudan University, Shanghai 200092, China.*

[c] *University of Chinese Academy of Sciences, Beijing 100049, China.*

[d] *School of Energy and Power Engineering, Jiangsu University of Science and Technology, Zhenjiang 212003, China.*

[e] *School of Materials Science and Engineering, Xi'an University of Science and Technology, Xi'an 710054, China.*

[f] *School of Chemical Engineering, The University of Adelaide, Adelaide, SA 5005, Australia.*

*Corresponding author

E-mail address: YFB0983@hotmail.com (F. Yu), yjwang@issas.ac.cn (Y. Wang)

Abstract

Multimetal oxide with asymmetric atomic sites offers potential solutions for Fenton-like reactions, while their pilot-scale synthesis remains challenging. Herein, we develop a continuous flash Joule heating method using a programmable logic controller with robotic arms to accomplish proof-of-concept of scalable production. The pilot-scale product (178.3 $\text{kg}\cdot\text{h}^{-1}\cdot\text{m}^{-2}$ electrode) of fusion ternary metal oxides was achieved for flow-through water treatment. Integrating multiple reaction electrodes with respective independent power further outlined an increased production path. Experiments and density functional theory calculations proved that fusion CuVFeO structure achieved the dual functionality of organics adsorption on Cu sites and peroxydisulfate activation on Fe sites. The synergistic reaction can be strengthened by V doping endowed with a d band center, leading to an increased Fe Bader charge. Therefore, triple site effects shorten the reaction distance between free radicals ($SO_4^{\bullet-}$ and •OH) and organics, enhancing free radicals' utilization and production efficiency. CuVFe secures superior performance during long-term operations (1455 min) in a continuous flow-through device. flash Joule heating characterization determined multi transition metals (CuVFe, CoVFe, MgVFe) can be generally synthesized with a superior catalytic performance. Undoubtedly, continuous flash Joule heating sheds light on developing advanced oxidation materials for pilot-scale wastewater treatment.

Keywords: Flash Joule heating, Multimetal oxide, Fenton-like, Pilot-scale synthesis.

1. Introduction

Transition metal oxides, such as spinel oxides, have become the best option for enhancing reaction oxygen species (ROS) productivity and utilization efficiency due to the structurally tunable [1–4]. For example, Fe–O–Mn superexchange interaction and the asymmetric tripe-atomic site (metal$_1$–oxygen–metal$_2$) contribute to the activation of the oxide agent due to the intermediate oxygen atom as a bridge for facilitating electron transfer [2,5]. In addition, multi-active sites have also been developed as different function sites, such as adsorption for organic pollutants and activation agents for oxygen [6–8]. However, multimetal catalysts, such as ternary metals or beyond, were usually prepared in conventional technology with a long-duration process (~hours), and the characteristics of materials are inferior due to phase separation and aggregation [9,10]. Meanwhile, such fancy materials cannot be scalable due to their low yield and tedious processes.

Current-induced flash Joule heating (FJH) technique has recently been conspicuous due to the distinct advantages for synthesizing various advanced materials [9,11,12]. Therefore, rapid heating and cooling in FJH reactions can promote the fusion of different metals, which is beneficial for enhancing the synergistic action of catalytic reactions [13,14]. However, the scalability of this technology still presents certain challenges [15]. Many researchers try to scale up reactors in a batch type [15]. However, this approach is inefficient for material production and usually leads to declined material performance due to the decreased power density. According to the equation ($p = \frac{1}{2m} C\ (U_2{}^2 - U_1{}^2)$, U2 and U1 represent the voltages before and after the reaction), power density (p) decreased with increased mass (m) at constant voltage [16,17]. As the mass of the precursor increases, the large-capacity capacitor box will increase multiplicatively to achieve a specific energy density. Consequently, increased current and unutilized energy can damage system circuits and components of FJH devices, which may pose potential safety hazards [18].

Recently, the roll-to-roll manufacturing for scalable production of materials would be realizable but remains envisaging [15,19]. From the batch type to continuing Joule heating production, how to automatically execute, the reactor size, the capacitor box capacity, and the selection of precursors would be significant for the material performances and smooth operation. Therefore, we developed a continuing Joule heating production with a suitable amplification reactor (bore size of quartz tube is 10 mm) by a programmable logic controller (PLC) platform with a robotic arm for achieving the proof-of-concept of scalable production [20]. Only upon completion of the proof-of-concept, the integration of multiple reaction electrodes corresponding to respective independent power in one device can be further effectively designed for scalable production.

In Fenton-like reaction, multivalent metals (especially for transition metals) are significant catalytic elements for activating oxidants to produce ROS, such as Fe, Cu, Co, Mn, Mo, V elements, and so forth [21]. Considering the abundance of Earth's elemental resources, cost-effectiveness, and environmental compatibility, this study selected Cu, V, and Fe elements as the focus of investigation. The metal-responding mechanism was elucidated by synthesizing various metal materials to achieve customized on-demand in advanced oxidation applications. The synthesis–structure–properties relationships, synergistic mechanism, and stability of performance and structure were also studied. Meanwhile, a continuous water treatment application was further developed to evaluate the practical applicability of the method.

2. Experimental section

2.1 Synthesis of ternary metal material by continuous FJH method

Compared to the batch-type FJH method, all processes were controlled by a PLC platform in the continuous FJH synthesis. To replace manual operations for achieving continuous synthesis, the following critical challenges must be addressed: ① How to accurately put the power sample into the react position; ② how to tightly compress the powder sample to achieve a closed circuit; ③ how to keep vacuum during the reacted process. Therefore, two robotic arm workstations were designed with an imputation algorithm based on locking the coordinates to accurately grasp the sample. In addition, we employed vertical placement and spring squeezing to achieve precise sample compression and circuit closure. Meanwhile, a vacuum chamber is utilized as the reactor, achieving a seal through rubber rings. Finally, the automation program was written using CANopen Builder 6.06software for PLC. Therefore, based on the PLC platform, integrating multiple modules, precisely coordinated with each other, can achieve all the steps to enhance production efficiency. Briefly, the precursor (0.2 g) was put into a quartz tube, the copper mesh was placed on both ends of the quartz tube, and one end of the quartz tube was placed on a copper electrode in the loading position. After completing the aforementioned steps, the continuous FJH equipment can be operated according to the designated procedure. We found the optimal synthetic condition was set at 250 V for 30 ms for ternary metal material (Cu, V, and Fe elements). To evaluate the stability of continuous FJH synthesis, we selected five batches of synthesized samples and assessed the performance and structural changes of these five batches of materials separately.

2.2 Materials synthesis by FJH for illuminating structure–property relationship

Hydrochar powder (0.5 g; detailed information was provided in Appendix A) with unitary, binary, and ternary metals (cupric acetate, vanadium chlorine, and hydroxydiacetyl iron powder, the total molar quantities were 2.8 mmol) were mixed with uniformity in deionized water by oscillation and then dried. Different metals from the binary and ternary materials were added with equivalent molar quantities. Finally, carbon black at 10 wt% was mixed with dried solids as different precursors for FJH treatment. The precursor (80 mg) was put into a quartz tube and compressed with copper electrodes to minimize the sample resistance as far as possible. Then, a mild vacuum (more than 38 kPa) was kept in the reaction chamber to avoid sample oxidation. Finally, different metal/carbon materials (Cu, V, Fe, CuV, CuFe, VFe, and CuVFe) were synthesized by the FJH method. The operation voltage and reaction time were 250 V and 30 ms three times.

2.3 Material Characterizations

X-ray absorption spectra (XAS), including X-ray absorption near-edge structure (XANES) and extended X-ray absorption fine structure (EXAFS), were analyzed for the different metal/carbon materials. The K-edge analyses of Cu, V, and Fe were performed with Si (111) crystal monochromators at the BL14W1 beamlines at the Shanghai Synchrotron Radiation Facility (SSRF; China).

Detailed information can be seen in Appendix A.

Density functional theory (DFT) calculation evaluated the adsorption configurations of S_2O_8, SO_4, and HSO_4 on the graphene-supported Fe_2CuO_4 (222) and V-doped Fe_2CuO_4 (222) since the (222) facets have been identified by high resolution transmission electron microscope (HRTEM; FEI Tecnai F20, USA). The mentioned heterostructures were constructed by graphene with a supercell (5 × 5) and Fe_2CuO_4 (222) with a supercell (1 × 1). In this case, the lattice mismatching is 3.8%, and graphene is wrinkled under compression. More detailed information can be seen in the supplementary information.

3. Results and Discussion

3.1 Proof-of-concept of scalable production by continuous FJH system.

A continuous Joule heating system was constructed for multimetal oxide materials (CuVFe as representative of the ternary metal oxides) to facilitate pilot-scale application. The diagrammatic sketch and practical view of the continuous Joule heating device for scale-up preparation are shown in Figs. S1 and S2 in Appendix A. All the processes were controlled by a PLC platform (Fig. 1(a)). Two robotic arm workstations for grasping samples significantly improved the production efficiency (Movie S1 in Appendix A). This method can produce material up to 178.3 $kg\cdot h^{-1}\cdot m^{-2}$ electrode (Table S1 in Appendix A). According to the material demand, the next-generation device's production rate can be further regulated via installment parallel reactors and independent power supply in a single apparatus (Fig. 1(b)). A reactor corresponding to an independent power for each reaction electrode can overcome the issues of reduced power density and interference between different reactors.

The reacted voltage and current indicated a similar variation trend (Fig. 1(c)). Meanwhile, all the maximum currents were about 260 A, indicating similar current-induced Joule heat and temperatures for breaking chemical bonds of precursors to produce active components. As anticipated, all the obtained materials exhibit an excellent and stable removal efficiency (above 90%) and are slightly different in the kinetics due to the difference in metal contents (Fig. 1(d) and Table S2 in Appendix A). The significant CuVFeO fusion structure (PDF No.75-1519 for Fe_2VO_4 and PDF No.01-077-0427 for $CuFe_2O_4$) was successfully synthesized (Fig. 1(e) and Fig. S3 in Appendix A). Meanwhile, Raman indicated the existing structure of few-layer graphene due to the ultra-high temperature and rapid cooling rate (Fig. S4 in Appendix A). Materials prepared by continuous Joule heating also have a similar surface area and pore size distribution (Fig. S5 and Table S3 in Appendix A). Therefore, it can be proved that the synthetic processes of continuous Joule heating for catalytic properties and multimetal oxide structure were stable in scale-up applications.

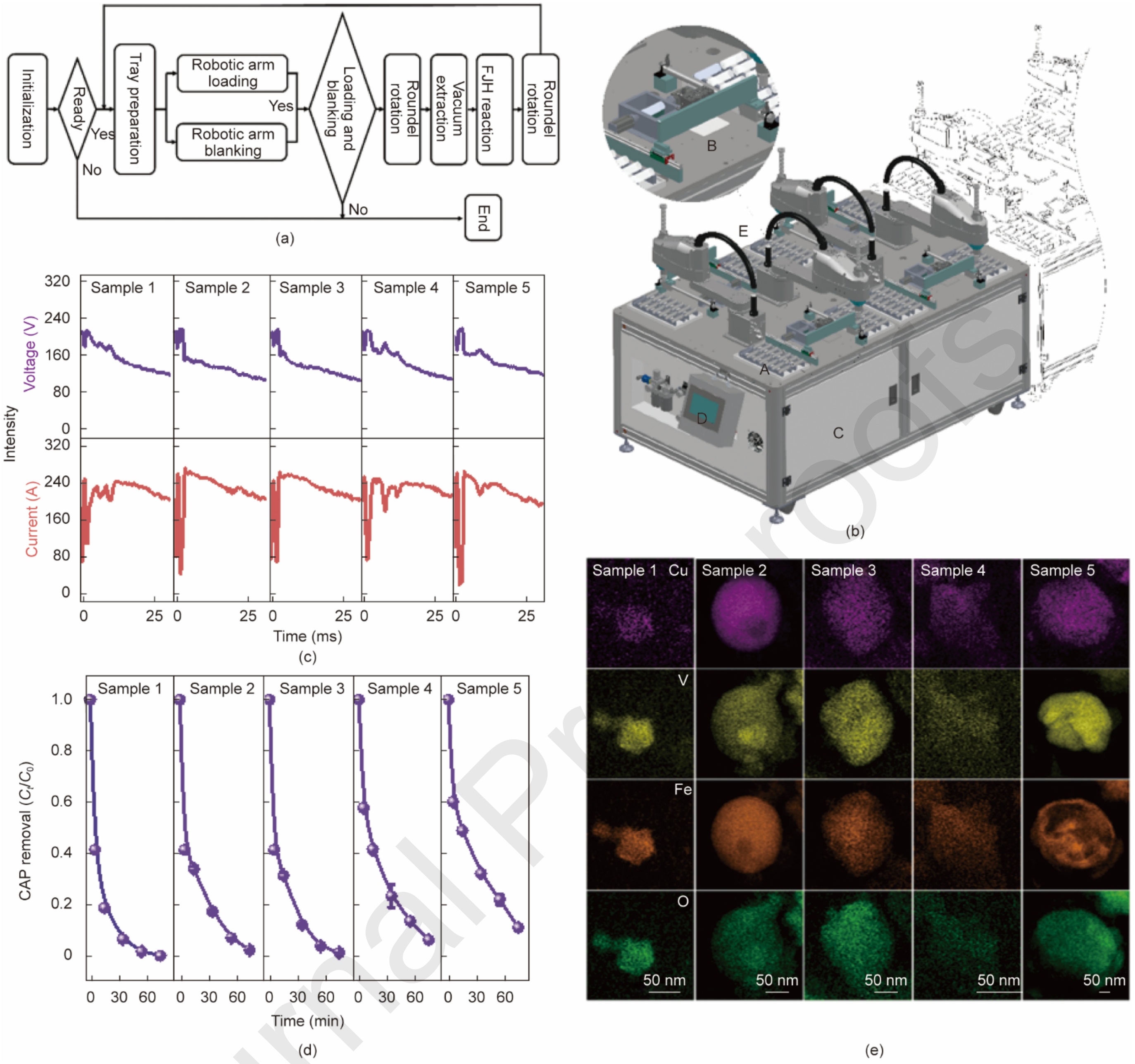

Fig. 1. (a) The logical framework of the continuous Joule heating method. (b) Diagrammatic sketch of updated continuous FJH synthesis was designed for improving production efficiency, which was constructed by the integration of multiple reaction electrodes with respective independent power. A: a loading area or collecting area, B: a reaction area (magnified view for reactor), C: corresponding to respective independent power in the interior of the device, D: PLC platform, and E: a robotic arm. (c) Recorded voltage and current of FJH continued synthesis processes to prepare ternary metal material (including Cu, V, and Fe elements) for five batches (samples 1–5). (d) CAP degradation profiles of ternary metal material prepared by continuous FJH method. Degradation conditions: $C_{\mathrm{CAP},0}$ = 60 mg·L^{-1}, C_{material} = 1000 mg·L^{-1}, C_{PDS} = 7 mmol·L^{-1}, initial pH$_0$ = 3.0 ± 0.2, temperature = 28 $^{\mathrm{o}}$C. The experiments were repeated twice. (e) TEM with an EDS pattern (different elements represent different colors) of ternary metal material prepared by continuous FJH method.

3.2 Synergistic activity of FJH-derived multimetal material.

After the proof-of-concept of scalable production, structure-property relationships were revealed to elucidate why ternary metal/carbon materials were used for catalytic reaction (Fig. 2(a)). Chloramphenicol (CAP) removal efficiency was found to be as follows: CuVFe or VFe > CuV or V > CuFe or Fe > Cu. CuVFe and VFe materials have excellent removal efficiency, especially regarding the kinetic rate constant (Fig. 2(b) and Fig. S6 in Appendix A). In addition, only Cu was inefficient for CAP removal according to the high metal Cu contents (Table S4 in Appendix A). CuVFe contains lower Fe and V contents than those of VFe, but has a similar CAP removal efficiency after adding the Cu element. Therefore, CuVFe material has a favorable structure for improving the CAP removal efficiency. We selected Cu (unary), CuV (binary), and CuVFe (ternary) materials as the main objects. The adsorption efficiencies of V, Cu, CuV, and CuVFe materials were 4.9%, 22.2%, 8.8%, and 9.5%, respectively (Fig. S7(a) and (b) in Appendix A). The Brunauer–Emmett–Teller (BET) surface areas of V, Cu, CuV, and CuVFe materials were 15.5, 18.5, 27.4, and 30.1 $m^2 \cdot g^{-1}$, respectively (Fig. S7(c) and Table S5 in Appendix A). N_2 adsorption isotherm exhibits a typical IV isotherm with H3 hysteresis loop, suggesting the presence of mesopores [22, 23]. The CAP adsorption was uncorrelated with the pore structure of materials (Fig. S7(d) in Appendix A). Therefore, Cu components in Cu-containing material would facilitate CAP adsorption, while CuV and CuVFe would decompose CAP via peroxydisulfate (PDS) activation [24,25].

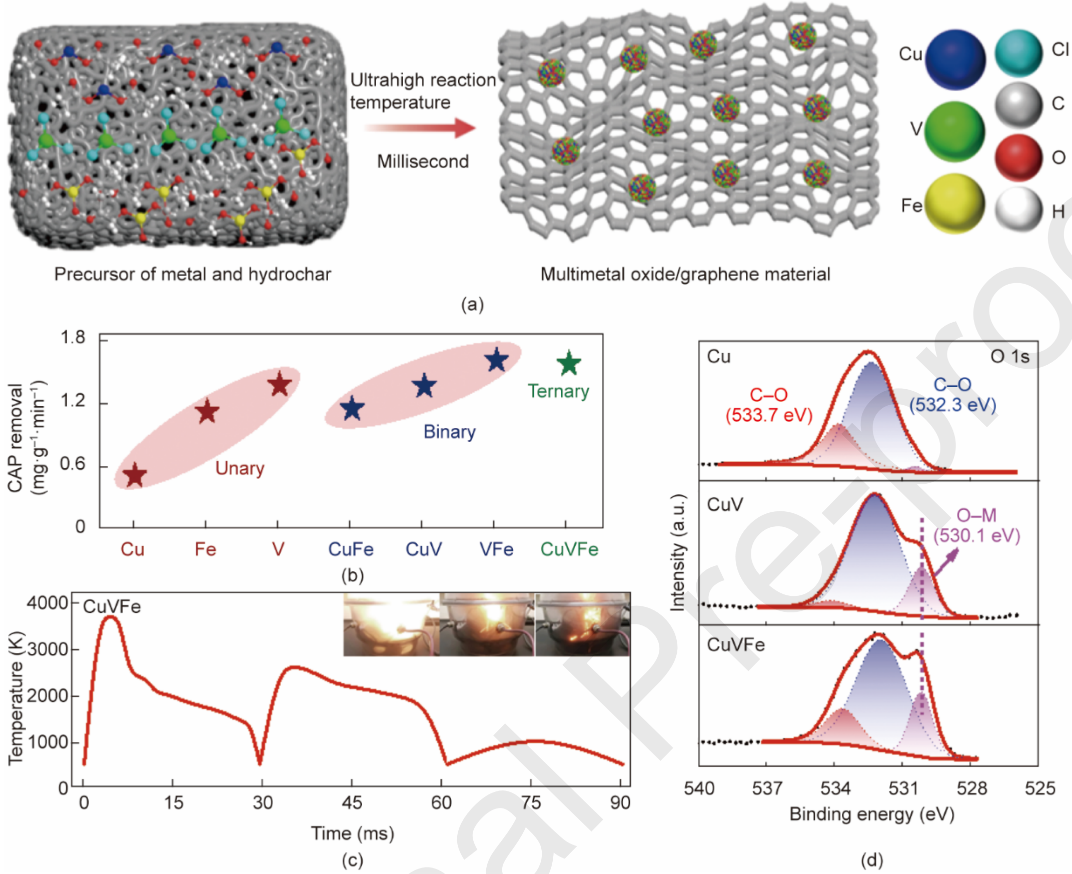

Fig. 2. (a) Synthesis processes of different metal/carbon materials prepared by FJH method, different elements represent different colors of the sphere. (b) The CAP removal performances of unary, binary, and ternary metal/carbon materials prepared by FJH. (c) Temperature changes of CuVFe material in the FJH process. (d) O 1s XPS spectra of Cu, CuV, and CuVFe materials prepared by FJH, M represent the metal elements.

3.3 FJH-derived fusion ternary metal oxide structure.

High active components can be induced by the current-derived ultra-high temperature (~3800 K within milliseconds; Figs. S8 and S9 in Appendix A and Fig. 2(c)) [26]. Regarding the morphology and microstructure, scanning electron microscope (SEM; Sigma 300, Germany) and transmission electron microscopy (TEM; FEI Tecnai F20, USA) show many sphere metal particles on the surface of the carbon substrate (Fig. S10 in Appendix A) [27]. The small metal particles were uniformly distributed with an average size of 46.2 nm for Cu, 33.0 nm for CuV, and 40.8 nm for CuVFe due to the rapid cooling (Fig. S11 in Appendix A) [28,29]. In addition, the metal and oxygen were distributed within the same particle characterized by TEM with an energy dispersive spectrometer (EDS), which indicated the existing fusion CuVO and CuVFeO structure (Fig. S12 in Appendix A). Meanwhile, the fusion CuVO and CuVFeO structures were further validated by the high-resolution TEM with EDS and ^{57}Fe Mössbauer spectroscopy (Figs. 2(d), 3(a), and 3(b) and Table S6 in Appendix A) [9,28,30,31].

Meanwhile, X-ray diffractometer (XRD; Smartlab, Japan) and selected area electron diffraction (SAED) results also indicated a binary metal oxide as CuVO ($Cu_{0.4}V_2O_5$, PDF No.46-0361) in CuV, ternary metal oxide as CuVFeO (PDF No.75-1519 for Fe_2VO_4 and PDF No.01-077-0427 for $CuFe_2O_4$) (Figs. S13 and S14 in Appendix A) [29]. It can be inferred that ultra-high temperatures can break the chemical bond of precursors to produce metallic oxide and promote the liquefaction of the metallic oxide, which can be solidified to form a multimetal oxide structure [29,32,33]. Meanwhile, Cu^0 and Cu_2O in Cu material, VC in CuV material, and partial VOx in CuVFe material were produced by rapid thermal decomposition and carbothermal reduction reactions [34–36].

X-ray photoelectron spectroscopy (XPS; Thermo Kalpha, USA) results also indicated that multimetal oxide was formed with increasing metallic elements (Fig. S15 and Table S7 in Appendix A) [37–39]. The reason was that the weaker oxidation resistance of metal and entropy-increasing contribute to synthesizing multimetal oxide [40,41]. X-ray absorption near-edge structure (XANES) spectra and fitting valence results further indicated the values of the chemical valence of Cu element in CuV and CuVFe were similar and situated between Cu foil and Cu_2O, suggesting the existing Cu–O and Cu–Cu bonds [42]. In the same way, the values of the chemical valence of V and Fe elements were close to the values of V_2O_5 and Fe_2O_3 (Fig. S16 in Appendix A). Cu–O and Cu–Cu bonds were also verified by Fourier-transformed k^3-weighted extended X-ray absorption fine structure (EXAFS) spectra, while the V–V and Fe–Fe bonds did not exist due to the radial distance shifting (Fig. S17 in Appendix A) [43,44]. Fitting results of EXAFS indicated that Cu–O, V–O/C, Cu–O–V, and Cu–Cu bonds existed in CuV, while the coordination number of Cu–Cu was lower than that of Cu foil because of the fusion CuVO structure (Fig. 3(c) and Tables S8–S10 in Appendix A). Similarly, the presence of metal–O and metal–O–metal bonds was confirmed, aligning with the XRD results attributed to the metal fusion processes occurring under ultra-high temperatures [9,39]. The wavelet transforms (WT) results were also consistent with those of the XANES and EXAFS analyses (Fig. S18 in Appendix A) [45]. All the above results indicated again that fusion CuVO and CuVFeO structures were formed in the FJH processes.

A high degree of graphitization for enhancing electron transfer was further confirmed by the weak D peaks for defect and strong G and 2D peaks for graphitization and layers (Fig. 3(d) and Fig. S19 in Appendix A) [11]. In addition, multilayer graphene can be shocked by the high current to form the few-layer graphene verified by the I_{2D}/I_G values, and I represnt the peak area (Table S11 in Appendix A) [46]. The linear sweep voltammetry and electrochemical impedance spectroscopy curves further proved the greater electron transfer ability of CuVFe than that of CuV and Cu due to higher catalytic ability (Fig. S20 in Appendix A and Fig. 3(e)). Meanwhile, adding PDS in CuVFe system can trigger a higher current due to PDS activation (Fig. 3(f)). In contrast, the current decreased upon adding CAP due to the rapid consumption of PDS-evolved reactive species. Therefore, FJH processes contributed to forming the fusion structure embedded in layered graphene, facilitating fast PDS activation and efficient removal of organic pollutants [2].

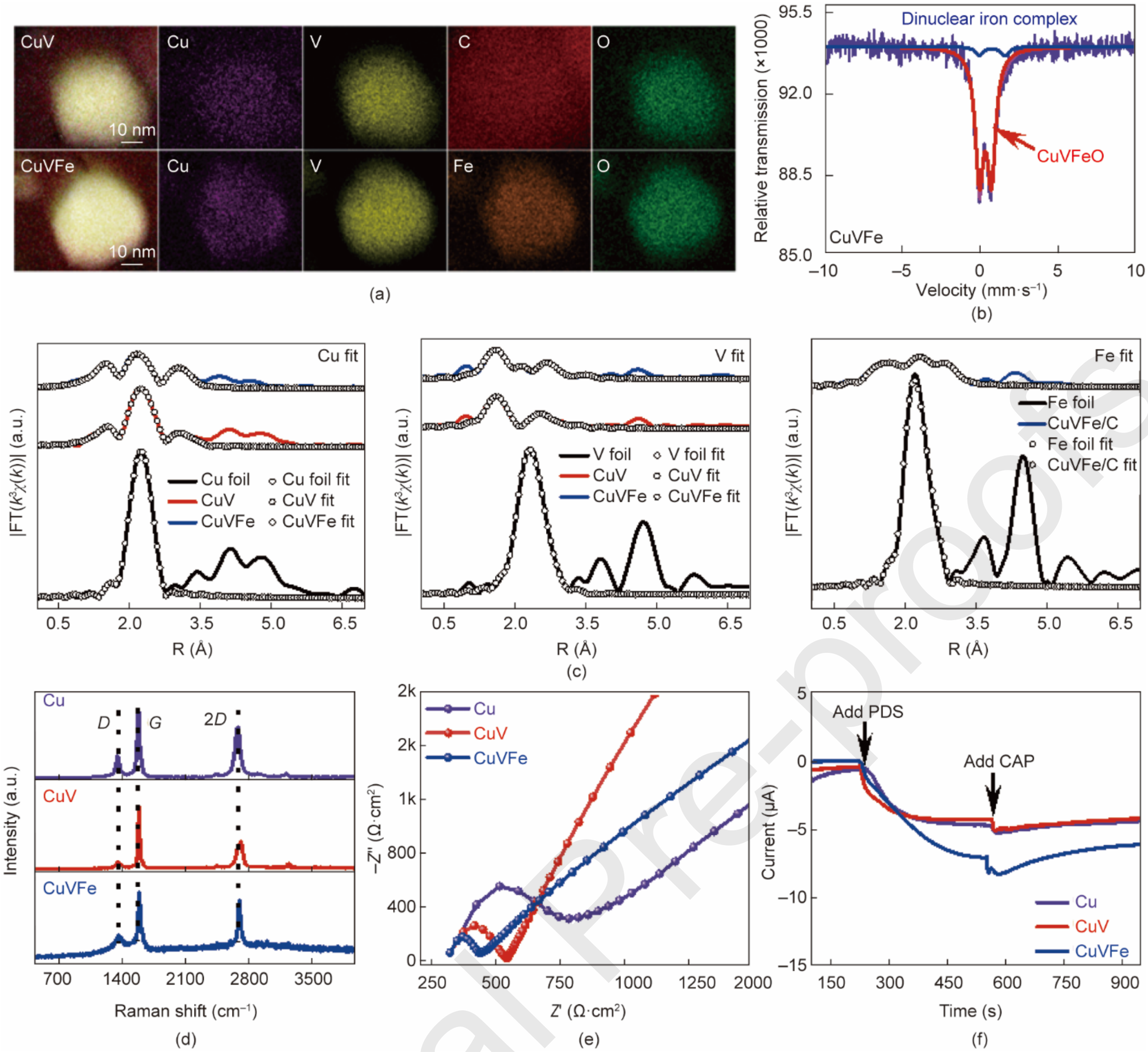

Fig. 3. (a) TEM with EDS patterns (different elements represent different colors) of CuV and CuVFe materials prepared by FJH. (b) Fe Mössbauer spectra of CuVFe material. (c) EXAFS fitting curves of CuV and CuVFe materials in R space. (d) Raman analysis, (e) electrochemical impedance spectroscopy curves, and (f) current (*I*)–time (*t*) curves of Cu, CuV, and CuVFe materials prepared by FJH. Z' and Z'' represent the real impedance.

3.4 Synergistic mechanism of fusion ternary metal oxides.

Electron paramagnetic resonance (EPR; Bruker EMXplus, Germany) illustrated a sequentially increased intensity of the •OH peak in Cu, CuV, and CuVFe, while the intensity of $^1O_2$ peak was similar (Fig. 4(a) and Fig. S21(a) in Appendix A). Results indicated that $^1O_2$ was produced by the self-decomposition of PDS, and only PDS demonstrated a minor contribution of CAP removal. The CAP removal experiments in D_2O system also indicated that $^1O_2$ was not the active species for CAP removal (Fig. S21(b) in Appendix A). Therefore, •OH may have dominantly contributed to CAP removal (Fig. 4(b)) [47]. The relationship between PDS activation and CAP removal efficiency further indicated that PDS consumption is independent of CAP addition, distinct from the nonradical electron transfer pathway, suggesting that CuVFe activated PDS to produce free radicals such as •OH (Fig. S21(c) in Appendix A and Fig. 4(c)). Quenching experiments illustrated that the •OH and $SO_4^{\bullet-}$ were the main active species for oxidation of CAP in the material surface (Fig. S22 in Appendix A). The absence of $SO_4^{\bullet-}$ in EPR may be that $SO_4^{\bullet-}$ existed in the material surface due to the strong adsorption ability and the slower capture efficiency of 5,5-dimethyl-1-pyrroline *N*-oxide (DMPO) for $SO_4^{\bullet-}$($k_{SO4\bullet-,\ DMPO} = 2.7 \times 10^{-2}$ $(mol \cdot L)^{-1} \cdot s^{-1}$ [48]) than that for •OH [48, 49]. Meanwhile, the rapid hydrolysis rate of highly unstable $DMPO^{\bullet}–SO_4^{-}$ into $DMPO^{\bullet}–OH$ via nucleophilic substitution [50]. The relative contribution of •OH was increased in CuV and CuVFe (Fig. 4(d)) [6,51]. In addition, the CAP removal rate by commercial VO_x and VC was lower than that of CuV and CuVFe (Fig. S23 in Appendix A). Therefore, it can be inferred that fusion structures (CuVFeO) were the dominant active metal sites for organic pollutant removal. The ratio of $Cu^{0/+}/Cu^{2+}$ and Fe^{2+}/Fe^{3+} were changed in the catalytic process, while the ratio of V^{3+}/V^{5+} was similar (Fig. S24 and Table S12 in Appendix A). It can be inferred that Fe site provided the electrons to PDS, while Cu site acquired the electrons from the organic pollutant during the catalytic process by the CuVFe material. V site may improve the coordination environment of Cu and Fe and contribute to activation efficiency. The Cu component was beneficial for CAP adsorption, as verified by the adsorption tests (Fig. S5(a)).

Furthermore, we used the same CuVFe precursor to prepare a CuVFe material by a conventional pyrolysis method. The CAP removal efficiency was inferior (43% removal efficiency) to that of the material prepared via FJH method (Fig. S25(a) in Appendix A). XRD illustrated that Fe_2VO_4 and Cu^0 were produced, while the fusion CuVFeO did not appear at a limited temperature for hours due to the low compatibility of Cu, V, and Fe (Fig. S25(b) in Appendix A). Meanwhile, a low degree of graphitization and aggregation existed (Fig. S25(c) in Appendix A), which led to a lower current than that of CuVFe prepared by FJH (Fig. S25(d) in Appendix A). According to the EPR, the CAP removal rate decreased due to the weak intensity of •OH (Fig. S26 in Appendix A). Therefore, the synergistic action in the fusion structure was achieved, which can improve the utilization and production efficiency of radicals.

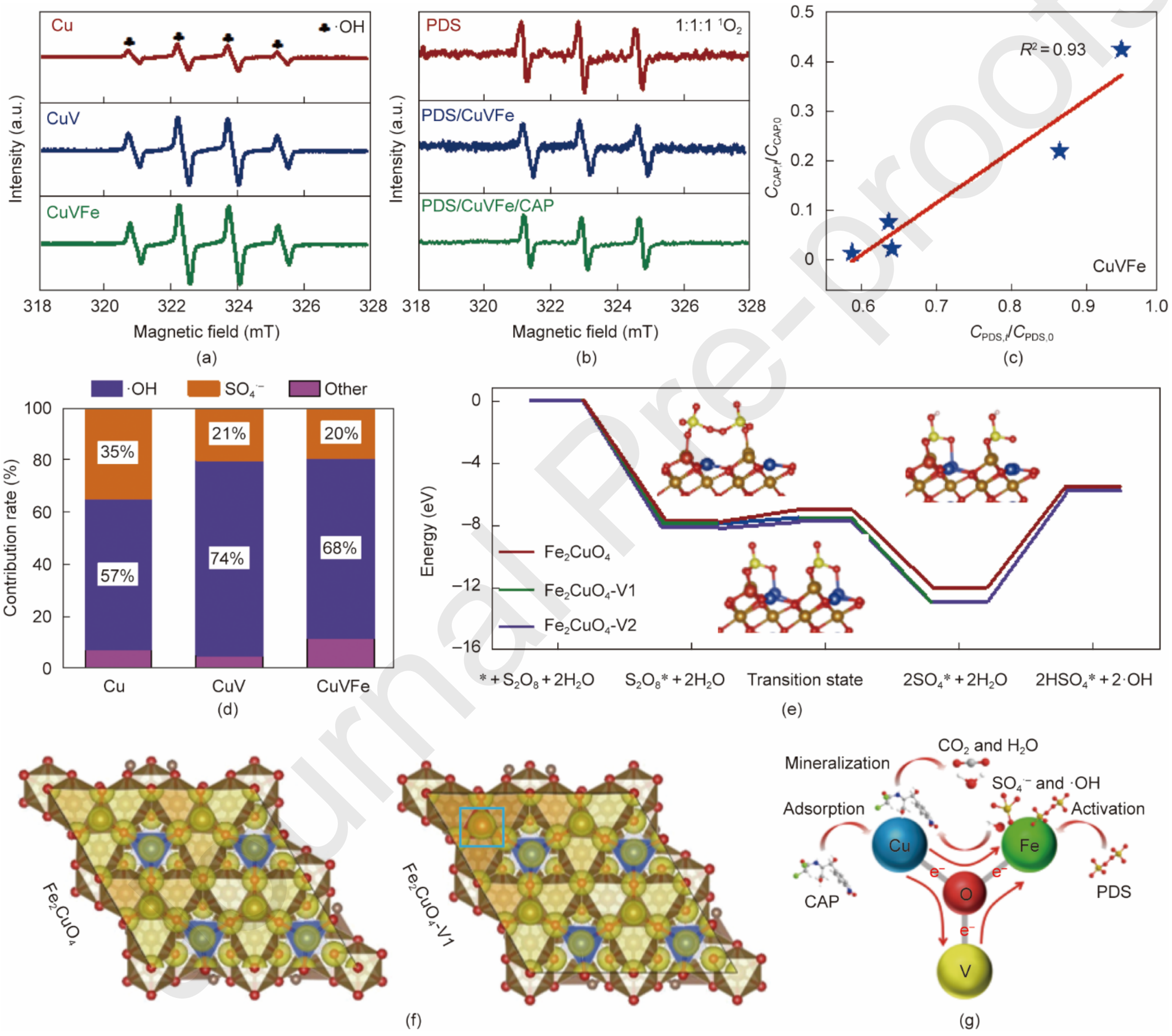

Fig. 4. (a) EPR spectra using DMPO as trapping reagents for •OH and $SO_4^{\bullet-}$. (b) EPR spectra using TEMP for $^1O_2$. (c) The linear relationship of PDS activation and CAP removal efficiency. (d) The contribution rate of different ROS by Cu, CuV, and CuVFe materials. (e) Energy profiles in different structures from material/S_2O_8 systems to material/2HSO_4 systems. Insert map representing Fe_2CuO_4-V1 structure. (f) The corresponding charge-density wave for Fe_2CuO_4 and Fe_2CuO_4-V1. (g) The catalytic mechanism of CuVFe for PDS activation and organic pollutant degradation in different elements.

3.5 Density functional theory (DFT) calculations.

Furthermore, we theoretically unraveled the importance of fusion CuVFeO structure in the PDS activation. To simplify the complexity of the structure, we referred to the XRD result of CuVFe material. The structures of Fe_2CuO_4/graphene, Fe_2CuO_4-V1/graphene, and Fe_2CuO_4-V2/graphene were established (Figs. S27–S29 in Appendix A), and Fe_2CuO_4-V1 and Fe_2CuO_4-V2 represented the substitution of V in different Fe atoms (V atom is in-frame in top view). The adsorption energy values of PDS on Fe_2CuO_4/graphene, Fe_2CuO_4-V1/graphene, and Fe_2CuO_4-V2/graphene systems were −7.77, −7.87, and −8.15 eV, respectively, indicating the substitution of V enhances the adsorption ability toward PDS activation [25]. The high adsorption ability also indicated strong adsorption for $SO_4^{\bullet-}$, which is consistent with the absence of $SO_4^{\bullet-}$ in EPR. Such deduction is further supported by the electron transfer from the catalytic material to PDS as well as the increased O-O bond length (Table S13 and Fig. S30 in Appendix A) [51,52]. Similarly, after the V substitution, the adsorption energy for SO_4 and HSO_4 was increased, which indicated that SO_4 adsorbed in material easily abstracts hydrogen from the solution system for the conversion from $SO_4^{\bullet-}$ to •OH [51,53].

We also evaluated the energy barrier of O–O bond breakage and found the lower energy barrier in the CuVFeO fusion structure. The energy barriers in PDS/Fe_2CuO_4-V1/graphene and PDS/Fe_2CuO_4-V2/graphene systems were 0.33 and 0.38 eV, respectively, while that of PDS/Fe_2CuO_4/graphene was 0.75 eV (Fig. S31(a) in Appendix A). Theoretically, a reaction with a reaction barrier less than 0.75 eV is expected to easily occur at room temperature [54]. It unveils the good activation ability of CuVFeO fusion structure toward PDS. Furthermore, the reduced reaction barriers supported the promotion effect by the V substitution toward O–O breakage (Fig. 4(e) and Fig. S31(b) in Appendix A). The improvement stems from the higher d band as well as the different electronegativity by the V dopant relative to the Fe element, which is evidenced by the upshifted d band center (Fig. S32 in Appendix A) and increased Bader charge at the Fe site (Fig. S33 in Appendix A). Thus, the Fe site, with a higher electron density, promotes its interactions with the peroxyl oxygen in PDS due to the strong interaction between V–O–Fe atoms (Fig. 4(f) and Fig. S33). Therefore, DFT calculations suggested that the fusion CuVFeO structure was important for activating PDS to produce the $SO_4^{\bullet-}$ and •OH. The catalytic mechanism can be proposed based on experimental results and density functional theory (DFT) calculations (Fig. 4(g)). Triple site effects can shorten the reaction distance between free radicals and organics. Meanwhile, asymmetric atomic sites (metal–O–metal) were beneficial for electron transfer to enhance free radicals' utilization and activation efficiency [2,6].

The possible by-products from CAP degradation were analyzed. Results indicated five by-products were produced (Table S14 in Appendix A). With the reaction time increasing, the peak area of CAP was decreased, while that of other intermediate products was increased, suggesting the CAP degradation. These intermediate products of small molecular components were produced by oxidation, dehydrogenation, cleavage of the amide group, and hydroxylation [25]. Importantly, these tiny molecular components were further mineralized into inorganic ions (such as CO_2, NO_3^- and Cl^-). Therefore, the proposed degradation pathway is shown in Fig. S34 in Appendix A.

In addition, different organic pollutants, including CAP, florfenicol (FF), sulfamethoxazole (SMX), and bisphenol A (BPA) were efficiently removed by the produced CuVFe (Fig. S35(a) in Appendix A). The removal efficiency of CuVFe material was also higher than other metal-based materials prepared by other methods (Fig. 5(a) and Table S15 in Appendix A). CuVFe material also has a universality for CAP removal in different pH and cyclic CAP degradation of CuVFe further indicated CAP removal was superior (over 95%) between cycle 2 (Figs. S35(b) and (c) in Appendix A). In the third cycle, the CAP removal rate rapidly decreased due to the substantial loss of active metal. Thus, FJH-derived CuVFe material has excellent removal efficiency for various organic pollutants and different pH systems, which is crucial for wastewater treatment due to the complex wastewater systems. In addition, FJH-derived material from different ternary metal/carbon precursors always presented superior CAP degradation efficiency (Fig. 5(b)), suggesting that FJH, as a state-of-the-art technology, held great scalable and general promise for mass production of nanostructured catalysts (CuVFe, CoVFe, MgVFe) for wastewater treatment.

Meanwhile, a wastewater treatment device and diagrammatic sketch of the scale-up treatment in the future are shown in Fig. S36 in Appendix A and Fig. 5(c). The CAP in lake water was treated, and the removal rate was achieved continuously at more than 90% for 1455 min with a stable flow rate (Fig. 5(d)). The material prepared by FJH method has a superb performance and stability for water pollutant removal. Meanwhile, the excellent synthetic stability, scalability, and removal efficiency illustrate that continuous Joule heating has significant practical application promise. Compared to the conventional methods such as pyrolysis and hydrothermal carbonization, FJH method enables instantaneous heating to 3400 ^{o}C, with the reaction completing within milliseconds (Fig. S37 in Appendix A). Ultra-high temperatures can break the chemical bond of precursors promote the liquefaction of the multimetal oxide, and further form a multimetal oxide within milliseconds. And FJH method also has a great potential application due to the higher product efficiency and lower energy consumption (Tables S16 and S17 in Appendix A).

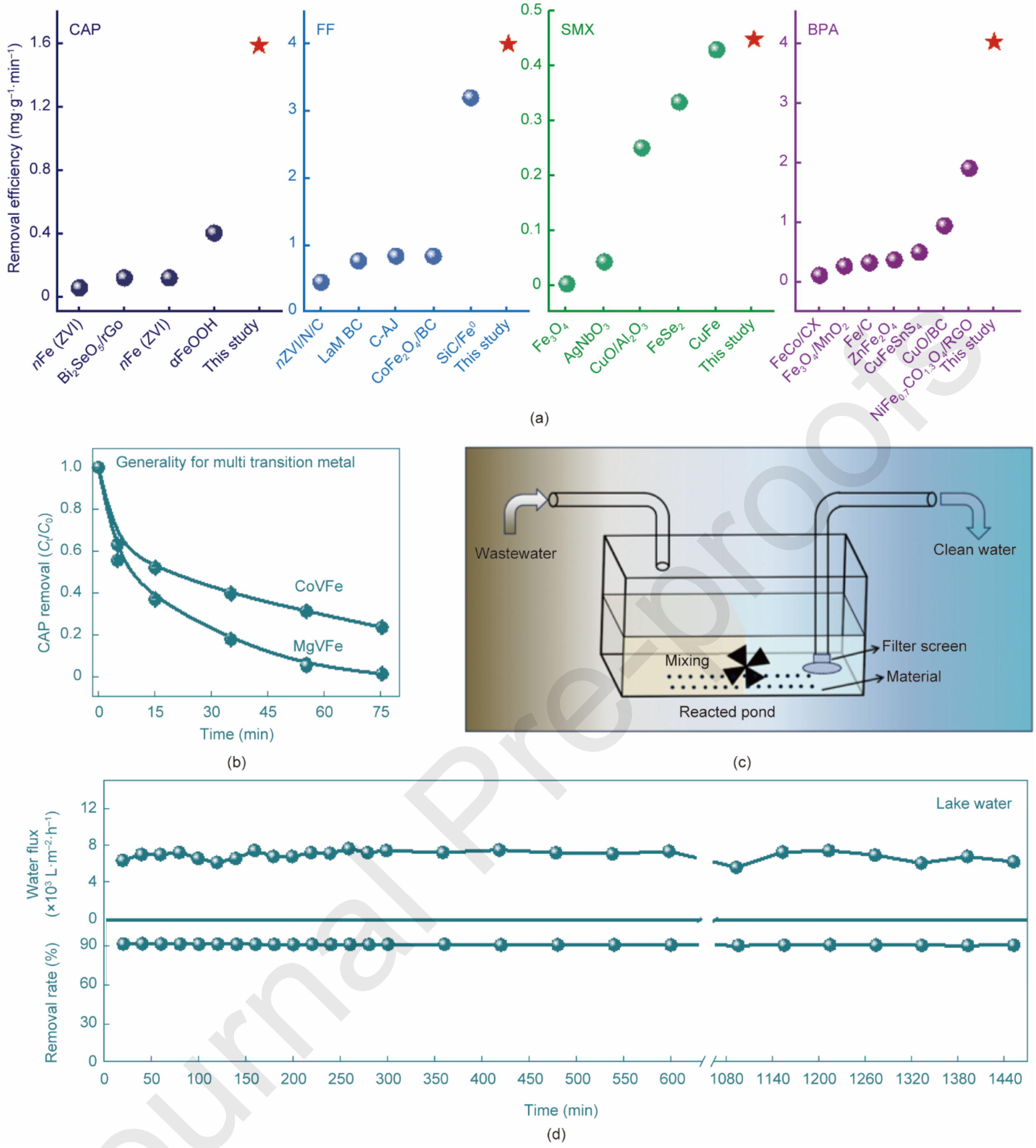

Fig. 5. (a) The comparison of removal performances of different organics of material prepared by conventional methods and FJH method. Detailed information can be shown in Table S15. (b) CAP degradation of CoVFe and MgVFe materials prepared by FJH method. Degradation conditions: $C_{CAP,0}$ = 60 mg·L^{-1}, $C_{material}$ = 1000 mg·L^{-1}, C_{PDS} = 7 mmol·L^{-1}, initial pH$_0$ = 3.0 ± 0.2, temperature = 28 °C. The experiments were repeated twice. (c) Diagrammatic sketch for continued wastewater treatment. (d) Treatment of CAP in lake water by CuVFe material in the homemade continue reactor. Degradation conditions: $C_{CAP,0}$ = 6 mg·L^{-1}, $C_{material}$ = 600 mg, C_{PDS} = 7 mmol·L^{-1}, initial pH$_0$ = 3.0 ± 0.2, temperature = 28 °C.

4. Conclusions

Proof-of-concept of scalable and general production was successfully achieved using a PLC-based continuous FJH method with a reactor corresponding to an independent power. In addition, the ultra-high temperature and rapid cooling rate can overcome their compatibility issues among multiple metal components for synthesizing fusion CuVFeO structures. CuVFe with a fusion structure can achieve synergistic PDS activation and pollutant removal coordinated by the triple catalytic sites. Fe catalyzes PDS activation and Cu serves as the pollutant adsorption site. DFT calculation theoretically confirmed that the substitution of V in different Fe atoms, Fe_2CuO_4-V1 and Fe_2CuO_4-V2 have a lower energy barrier for breaking the peroxyl O–O bond and higher adsorption energy for PDS with more electron transfer to evolve radical species. More importantly, the continuous-flowing systems integrating mass catalyst production and modification, along with catalytic wastewater treatment, exhibit high purification efficiency and stability, showing great potential for practical application.

Acknowledgments

This work was supported by the National Natural Science Foundation of China (42225701). We especially appreciate the XAFS measurements provided by the Shanghai Synchrotron Radiation Facility.

References

[1] Huang M, Li YS, Zhang CQ, Cui C, Huang QQ, Li M, et al. Facilely tuning the intrinsic catalytic sites of the spinel oxide for peroxymonosulfate activation: from fundamental investigation to pilot-scale demonstration. Proc Natl Acad Sci USA 2022;119(30):e2202682119.

[2] Guo ZY, Si Y, Xia WQ, Wang F, Liu HQ, Yang C, et al. Electron delocalization triggers nonradical Fenton-like catalysis over spinel oxides. Proc Natl Acad Sci USA 2022;119(31):e2201607119.

[3] Guo ZY, Sun R, Huang Z, Han X, Wang H, Chen C, et al. Crystallinity engineering for overcoming the activity–stability tradeoff of spinel oxide in Fenton-like catalysis. Proc Natl Acad Sci USA 2023;120(15):e2220608120.

[4] Lv W, Li H, Wang J, Wang L, Wu Z, Wang Y, et al. Mass transfer-promoted Fe^{2+}/Fe^{3+} circulation steered by 3D flow-through co-catalyst system toward sustainable advanced oxidation processes. Engineering 2024;36:264–75.

[5] Zhou Q, Song C, Wang P, Zhao Z, Li Y, Zhan S. Generating dual-active species by triple-atom sites through peroxymonosulfate activation for treating micropollutants in complex water. Proc Natl Acad Sci USA 2023;120(13):e2300085120.

[6] Li X, Huang X, Xi S, Miao S, Ding J, Cai W, et al. Single cobalt atoms anchored on porous N-doped graphene with dual reaction sites for efficient Fenton-like catalysis. J Am Chem Soc 2018;140(39):12469–75.

[7] Cao W, Hu C, Lyu L. Efficient decomposition of organic pollutants over *n*ZVI/FeO*x*/FeN*y*-anchored NC layers via a novel dual-reaction-centers-based wet air oxidation process under natural conditions. ACS EST Engg. 2021;1(9):1333–41.

[8] Zhang T, Liu Z, Ye Y, Wang Y, Yang H, Gao H, et al. Dry reforming of ethane over FeNi/Al–Ce–O catalysts: composition-induced strong metal-support interactions. Engineering 2022;18:173–85.

[9] Yao Y, Huang Z, Xie P, Lacey SD, Jacob RJ, Xie H, et al. Carbothermal shock synthesis of high-entropy-alloy nanoparticles. Science 2018;359(6383):1489–94.

[10] Ahn J, Park S, Oh D, Lim Y, Nam JS, Kim J, et al. Rapid Joule heating synthesis of oxide-socketed high-entropy alloy nanoparticles as CO_2 conversion catalysts. ACS Nano 2023;17(13):12188–99.

[11] Luong DX, Bets KV, Algozeeb WA, Stanford MG, Kittrell C, Chen W, et al. Gram-scale bottom-up flash graphene synthesis. Nature 2020;577(7792):647–51.

[12] Park S, Jiang T, Zheng K, Lin Z, Meng Y, Wang M, et al. Ultrafast thermal synthesis of non-noble metal-based electrocatalysts for overall water splitting. ACS Appl Energy Mater 2023;6(11):5787–5796.

[13] Chen J, Ma Y, Huang T, Jiang T, Park S, Xu J, et al. Ruthenium-based binary alloy with oxide nanosheath for highly efficient and stable oxygen evolution reaction in acidic media. Adv Mater 2024;36(26):e2312369.

[14] Jiang T, Liu Z, Yuan Y, Zheng X, Park S, Wei S, et al. Ultrafast electrical pulse synthesis of highly active electrocatalysts for beyond-industrial-level hydrogen gas batteries. Adv Mater 2023;35(32):e2300502.

[15] Wyss KM, Luong DX, Tour JM. Large-scale syntheses of 2D materials: flash Joule heating and other methods. Adv Mater 2022;34(8):e2106970.

[16] Liu Y, Tian X, Han Y, Chen Y, Hu W. High-temperature shock synthesis of high-entropy-alloy nanoparticles for catalysis. Chin J Catal 2023;48:66–89.

[17] Han Y, Cao P, Tian Z. Controllable synthesis of solid catalysts by high-temperature pulse. Acc Mater Res 2023;4(8):648–54.

[18] Ramírez J, Yépez E, Pantoja Suárez F, Acurio E, Pérez F, Basile L. Design and construction of a high-current capacitor bank for flash graphene synthesis. Engineering Proceedings 2023;47(1):18.

[19] Zhang W, Wei X, Wu T, Wei F, Ma L, Lv Y, et al. Carbothermal shock enabled functional nanomaterials for energy-related applications. Nano Energy 2023;118:108994.

[20] Zhu X, Lin L, Pang M, Jia C, Xia L, Shi G, et al. Continuous and low-carbon production of biomass flash graphene. Nat Commun 2024;15(1):3218.

[21] Zhu ZS, Zhong S, Cheng C, Zhou H, Sun H, Duan X, et al. Microenvironment engineering of heterogeneous catalysts for liquid-phase environmental catalysis. Chem Rev 2024;124(20):11348–434.

[22] Bi F, Wei J, Gao B, Liu N, Xu J, Liu B, et al. New insight into the antagonism mechanism between binary VOCs during their degradation over Pd/ZrO_2 catalysts. ACS EST Engg. 2024;4(6):1346–55.

[23] Gao B, Bi F, Zhou Z, Zhang Y, Wei J, Lv X, et al. A bimetallic MOF-derived MnCo spinel oxide catalyst to enhance toluene catalytic degradation. Chem Commun (Camb) 2024;60(58):7455–8.

[24] Fang G, Deng Y, Huang M, Dionysiou DD, Liu C, Zhou D. A mechanistic understanding of hydrogen peroxide decomposition by vanadium minerals for diethyl phthalate degradation. Environ Sci Technol 2018;52(4):2178–85.

[25] Yu F, Jia C, Wu X, Sun L, Shi Z, Teng T, et al. Rapid self-heating synthesis of Fe-based nanomaterial catalyst for advanced oxidation. Nat Commun 2023;14(1):4975.

[26] Yao Y, Liu Z, Xie P, Huang Z, Li T, Morris D, et al. Computationally aided, entropy-driven synthesis of highly efficient and durable multi-elemental alloy catalysts. Sci Adv 2020;6(11):eaaz0510.

[27] Sun Y, Ma C, Wu D, Liu X, Li N, Fan X, et al. Coating $CoFe_2O_4$ shell on Fe particles to increase the utilization efficiencies of Fe and peroxymonosulfate for low-cost Fenton-like reactions. Water Res 2023;244:120542.

[28] Baek J, Hossain MD, Mukherjee P, Lee J, Winther KT, Leem J, et al. Synergistic effects of mixing and strain in high entropy spinel oxides for oxygen evolution reaction. Nat Commun 2023;14(1):5936.

[29] Fan J, Zhang X, Han M, Xiang X, Guo C, Lin Y, et al. Amorphous Ni–Fe–Mo oxides coupled with crystalline metallic domains for enhanced electrocatalytic oxygen evolution by promoted lattice-oxygen participation. Small 2024;20(10):e2303927.

[30] Permer L, Laligant Y, Ferey G, Calage Y. Crystal structure, magnetic, and Mössbauer studies of $Cu_6Fe_{0.9}V_6O_{19}$: a compound with relaxation effect. J Solid State Chem 1993;107(2):539–546.

[31] Wang S, Wang J, Xu H. Discrepant catalytic activity of biochar-based Fe and Co homonuclear and heteronuclear diatomic catalysts for activating peroxymonosulfate to degrade emerging pollutants. ACS EST Engg 2024;4(7):1758–68.

[32] Cai M, Wang X, Xue J, Jiang Y, Wei Y, Cheng Q, et al. Improvement of photocatalytic hydrogen evolution of $La_5Ti_2AgS_5O_7$ by flash sintering method. Appl Phys Lett 2021;119(7):1–6.

[33] Li T, Yao Y, Ko BH, Huang Z, Dong Q, Gao J, et al. Carbon-supported high-entropy oxide nanoparticles as stable electrocatalysts for oxygen reduction reactions. Adv Funct Mater 2021;31(21):2010561.

[34] Yang Q, Ma X, Li Y, Jiang L, Chen D, He J, et al. One-pot pyrolysis and enhanced efficient solar evaporation of Cu/Cu_2O/biochar. Mater Today Sustain 2023;22:100363.

[35] Li C, Wang Z, Liu M, Wang E, Wang B, Xu L, et al. Ultrafast self-heating synthesis of robust heterogeneous nanocarbides for high current density hydrogen evolution reaction. Nat Commun 2022;13(1):3338.

[36] Song JY, Kim C, Kim M, Cho KM, Gereige I, Jung WB, et al. Generation of high-density nanoparticles in the carbothermal shock method. Sci Adv 2021;7(48):eabk2984.

[37] Lyu Z, Zhu S, Xie M, Zhang Y, Chen Z, Chen R, et al. Controlling the surface oxidation of Cu nanowires improves their catalytic selectivity and stability toward C_{2+} products in CO_2 reduction. Angew Chem Int Ed Engl 2021;60(4):1909–15.

[38] Sun L, Wu X, Jiao Y, Jia C, Teng T, Lin L, et al. Millisecond self-heating and quenching synthesis of Fe/carbon nanocomposite for superior reductive remediation. Appl. Catal. B: Environ. Energy 2024;342:123361.

[39] Liao Y, Zhu R, Zhang W, Zhu H, Sun Y, Chen J, et al. Transient synthesis of carbon-supported high-entropy alloy sulfide nanoparticles via flash Joule heating for efficient electrocatalytic hydrogen evolution. Nano Res 2024;17(4):3379–89.

[40] Li T, Yao Y, Huang Z, Xie P, Liu Z, Yang M, et al. Denary oxide nanoparticles as highly stable catalysts for methane combustion. Nat Catal 2021;4(1):62–70.

[41] Reed TB. Free energy of formation of binary compounds. Cambridge: MIT Press; 1971.

[42] Grosse P, Gao D, Scholten F, Sinev I, Mistry H, Roldan Cuenya B. Dynamic changes in the structure, chemical state and catalytic selectivity of Cu nanocubes during CO_2 electroreduction: size and support effects. Angew Chem Int Ed Engl 2018;130(21):6300–5.

[43] Zhang G, Xiong T, Pan X, Zhao Y, Yan M, Zhang H, et al. Illumining phase transformation dynamics of vanadium oxide cathode by multimodal techniques under operando conditions. Nano Res 2019;12(4):905–10.

[44] Yang Q, Fu X, Jia C, Ma C, Wang X, Zeng J, et al. Structural determination of catalytically active subnanometer iron oxide clusters. ACS Catal 2016;6(5):3072–82.

[45] Hu F, Yu D, Ye M, Wang H, Hao Y, Wang L, et al. Lattice-matching formed mesoporous transition metal oxide heterostructures advance water splitting by active Fe–O–Cu bridges. Adv Energy Mater 2022;12(19):2200067.

[46] Hwangbo Y, Lee C, Mag-Isa AE, Jang J, Lee H, Lee S, et al. Interlayer non-coupled optical properties for determining the number of layers in arbitrarily stacked multilayer graphenes. Carbon 2014;77:454–61.

[47] Wu JH, Chen F, Yang TH, Yu HQ. Unveiling singlet oxygen spin trapping in catalytic oxidation processes using *in situ* kinetic EPR analysis. Proc Natl Acad Sci USA 2023;120(30):e2305706120.

[48] Wei Z, Villamena FA, Weavers LK. Kinetics and mechanism of ultrasonic activation of persulfate: an *in situ* EPR spin trapping study. Environ Sci Technol 2017;51(6):3410–7.

[49] Qin W, Fang G, Wang Y, Zhou D. Mechanistic understanding of polychlorinated biphenyls degradation by peroxymonosulfate activated with $CuFe_2O_4$ nanoparticles: key role of superoxide radicals. Chem Eng J 2018;348:526–34.

[50] Zou J, Ma J, Zhang J. Comment on electrolytic manipulation of persulfate reactivity by iron electrodes for TCE degradation in groundwater. Environ Sci Technol 2014;48(8):4630–1.

[51] Lee J, von Gunten U, Kim JH. Persulfate-based advanced oxidation: critical assessment of opportunities and roadblocks. Environ Sci Technol 2020;54(6):3064–81.

[52] Wu X, Kim J. Outlook on single atom catalysts for persulfate-based advanced oxidation. ACS EST Engg. 2022;2(10):1776–96.

[53] Liang C, Su H. Identification of sulfate and hydroxyl radicals in thermally activated persulfate. Ind Eng Chem Res 2009;48(11):5558–62.

[54] Shang C, Liu Z. Origin and activity of gold nanoparticles as aerobic oxidation catalysts in aqueous solution. J Am Chem Soc 2011;133(25):9938–47.

Declaration of interests

☒ The authors declare that they have no known competing financial interests or personal relationships that could have appeared to influence the work reported in this paper.

☐ The author is an Editorial Board Member/Editor-in-Chief/Associate Editor/Guest Editor for *[Journal name]* and was not involved in the editorial review or the decision to publish this article.

☐ The authors declare the following financial interests/personal relationships which may be considered as potential competing interests: